MACHINE SCIENCE

ISSN: 2227-6912
E-ISSN: 2790-0479

2022, Volume 11, № 2. Pages 54 – 70

A CONSTANT VOLUMETRIC-FAILURE-STRAIN EROSION FOR DETERMINING THE EFFECT OF INERTIA AND STRAIN RATE ON THE CRUSHING STRENGTH OF A CELLULAR CONCRETE

Burak AKYOL[1], Mustafa GÜDEN[2*]

[1,2]Dynamic Testing and Modeling Laboratory and Department of Mechanical Engineering, Izmir Institute of Technology, Izmir, Turkey

E-mail:bakyol@iyte.edu.tr[1], mustafaguden@iyte.edu.tr[2]*

Abstract: The effect of inertia and strain rate on the failure of a cellular autoclaved aerated concrete (600 kg m^{-3}) was investigated using MAT_096 material model together with a constant volumetric-failure-strain erosion criterion in the LSDYNA. A rate insensitive, constant compressive yield stress, and a rate sensitive, variable compressive yield stress, model were implemented and the results of models were compared with those of experimental compression tests conducted at similar strain rates, between $2x10^{-3}$ s^{-1} and ~4150 s^{-1}. Results have shown an "s-type" compressive strength relation with strain rate, broadly composing of three distinct regions: a lower-velocity-dependent-strength region at the quasi-static velocities, a higher-velocity-dependent-strength region at intermediate velocities and again a lower-velocity-dependent-strength region above ~1150 s^{-1}. In experimentally tested samples, a shock fracture strength was presumed to be reached in the higher velocity-dependent strength region, resulting in a cut-off DIF value (2.78), while in numerically tested samples, the compressive strength increased with increasing strain rate in the third region. One dimensional state of strain condition above a critical velocity was also shown numerically. The stress triaxiality increased to 0.66 between 1 and 30 m s^{-1}, reaching a fully constraint 1D state of strain condition above 30 m s^{-1}. In accord with this, the numerical failure mode, as with that of experiments, switched from an axial- to a radial-dominated cracking after ~20 m s^{-1}. Finally, the strain rate dependent compressive strength was numerically shown as partly arising due to the change of deformation state from a 1D state of stress to a 1D state of strain and partly due to the intrinsic rate sensitivity of cellular concrete.

Keywords: *Autoclaved aerated concrete, modelling, compressive strength, inertia, strain rate*

Introduction. There have been numerous experimental and numerical investigations on the strain rate dependent compressive strength of concrete. A summary on the strain rate dependent compressive strength of concrete can be found in a recent review article [1]. Briefly, the dynamic increase factor (DIF=dynamic facture strength/static fracture strength) of concrete varies between 1 and 2.5, from static to dynamic strain rates, with a sudden increase after about 100 s^{-1} [1]. A relatively low dependence of DIF on strain rate until about 100 s^{-1} was ascribed to both the strain-rate dependent growth of tensile micro cracks, known as thermally activated facture mechanism, and the viscous behavior of the bulk material between cracks known as Stefan effect [2-4]. The thermally activated facture mechanism is explained as follows. The energy needed for crack opening is much higher than the energy needed for crack growth at quasi-static strain rates. While, there is less time at high strain rates for both crack opening and growth, causing an increase in fracture strength and the number of micro cracks formed as compared with quasi-static strain rates. It was argued that inertial effects become predominant at the strain rates higher than 10 s^{-1} [5]. At increasing strain rates, an elastically deforming structure cannot expand in transverse direction (Poisson's expansion) due to radial inertia restraint. Radial inertia imposes a confinement pressure on deforming structure, transforming the deformation from a uniaxial state of stress to a uniaxial state of strain. The rapid increase of the strength of concrete after about a critical strain rate is therefore ascribed to the development of a uniaxial state of strain [6-10]. The variations in the DIF values of different studies performed at similar strain rates were further attributed to the variations in the extent of radial and axial inertia between the concrete samples tested [11, 12]. The reported data on the compressive strength of concrete included the forces due to both axial and radial inertia.

An "s-type" dependence of the fracture strength of brittle materials on strain rate was reported [13]. On an "s-type" curve, there are two turning points: (1) from a low-strain rate-dependent strength region to a high-strain rate-dependent strength region and (2) from a high-strain rate-dependent strength region to again a low-strain rate-dependent strength region. The strength of limestone increased slowly with increasing strain rate up to 10^3 s^{-1}; thereafter, increased sharply, approaching the shock fracture strength [6]. The strain rate dependent fracture strength well above 10^3 s^{-1} was proposed to resemble the strain dependent fracture strength below 10^3 s^{-1}, while the rapid increase of fracture strength around 10^3 s^{-1} was ascribed to the transformation of deformation from a uniaxial state of stress to a uniaxial state of strain. The first and second turning points were reported sequentially 10^2 and 10^4 s^{-1} for concrete [14]. Also, in accord with above, the current concrete models have recently adapted a cut-off value of 2.94 to cap DIF above 300 s^{-1} [15]. But, it is not clear whether or not this capping occurs in or after the high-strain rate-dependent strength region. Alternatively, it is proposed that the capping may occur because concrete reaches its ultimate dynamic strength before the second turning point in the high-strain rate-dependent strength region [4].

The aim of this study was to experimentally and numerically investigate the strain rate sensitive compressive strength of an aerated autoclaved concrete (AAC) using a constant volumetric-failure-strain erosion criterion in the MAT_096 material model of the LSDYNA. Once an element reached a critical volumetric-failure-strain corresponding to that of quasi-static strain rate it was eroded. The used erosion criterion and the associated material model were relatively simple, requiring few experimental input parameter and noted to predict the trends of experimental stress-strain curves with strain rate. The model results were further verified with the compression test results between quasi-static ($2x10^{-3}$ s^{-1}) and dynamic (~4150 s^{-1}) strain rates. Modified Split Hopkinson Pressure Bar (SHPB) tests, so called the direct impact tests, were performed to achieve strain rates above 1000 s^{-1}. Two different modelling approach called Model 1 and Model 2 were investigated. In the first, a strain rate independent material model was implemented to determine the effect of axial and radial inertia on the fracture strength merely. In the second, a strain rate dependent compressive strength was used as an input to the material model to show the effect of strain rate. Since the investigated upper dynamic strain rates were higher than those of the second turning point of concrete on an "s-type" curve, the model and experimental results allowed the analysis of the strain rate dependent-fracture strength at above these critical strain rates using both approach. Finally, as there has been, so far, no numerical studies on the strain rate dependent compressive strength of these materials and few experimental investigation on the dynamic response [16-19], the results of present study are expected to contribute to the knowledge on modelling dynamic mechanical response of such brittle cellular materials.

Tests and models.

Tests

Quasi-static and dynamic compression test samples were ~19.4 mm in diameter and 26 mm in length. The test samples' diameter was determined by the bar diameter of the used SHPB. Quasi-static compression tests were performed in a Shimadzu AG-X Universal Test machine at $5x10^{-5}$, $5x10^{-4}$, and $5x10^{-3}$ m s^{-1}, corresponding to strain rates of ~$2x10^{-3}$, ~$2x10^{-2}$ and ~$2x10^{-1}$ s^{-1}, respectively. Low-velocity compression tests were performed in a FRACTOVIS drop-weight test device using a flat-ended striker at about 1 m s^{-1}, corresponding to a strain rate of ~35 s^{-1}. The dynamic compression tests were performed in a SHPB apparatus, having 19.4 mm-diameter Inconel 718 incident (3110 mm) and transmitter (2050 mm) bars. Conventional SHPB compression tests were performed at 8 m s^{-1} corresponding to ~185 s^{-1}. In the direct impact tests, the striker bar (Inconel bar 500 mm-long and aluminum bar 200 mm-long) directly impinged on the test sample inserted to the end of the SHPB incident bar. The direct impact SHPB tests were performed at 10, 30 and 108 m s^{-1} corresponding to ~385, ~1150 and ~4150 s^{-1}, respectively. At least 8 samples were tested at each strain rate. The details of the direct impact tests and the used SHPB test device are given elsewhere [20-22]. The tensile strength of AAC sample was determined by the indirect tensile Brazilian tests. In these tests, the cylindrical compression test samples (3 tests), 19.4 mm in diameter and 26 mm in length, were compressed laterally in a Shimadzu AG-X Universal Test Machine. The tensile strength (σ_t) was then calculated as

$$\sigma_t(t) = \frac{2P}{\pi DL} \quad (1)$$

where P, D and L are sequentially the fracture load and the diameter and thickness of sample.

Models

The quasi-static and high strain rate compression and direct impact tests were simulated in the non-linear explicit finite element code of LS-DYNA. The quasi-static model was briefly composed of top and bottom compression test platen (tool steel) and sample as seen in Figure 1(a). Each compression platen was modelled using 6 mm-long and 2 mm–wide 19200 solid elements and MAT020_RIGID material model (E=210 GPa and v=0.3). The rotations and the translations of compression test platens were restricted in all directions, except the axial translation of the top platen in z-direction was kept constant by PRESCRIBED_MOTION_RIGID card at 5x10^{-3} m s^{-1}, the same as the quasi-static tests. The contacts between compression test platens and sample were defined by AUTOMATIC_SURFACE_TO_SURFACE. The mass scaling was implemented in the quasi-static simulation by using CONTROL_TIMESTEP card. The model was initially simulated without mass scaling in order to determine time-step. The determined time-step was then multiplied by a factor until kinetic energy became much smaller than internal energy. A mass scaling factor of 1000 was determined by following above procedure. In the SHPB test model, the striker, incident and transmitter bars were modelled using 15x2 mm 7000, 28980 and 19180 solid elements, respectively (Figure 1(b)). The striker bar velocities in the SHPB model were 1 and 8 m s^{-1}. The drop-weight test at ~1 m s^{-1} was also modelled with the SHPB compression test model. The lengths of Inconel 718 striker, incident and transmitter bar were sequentially 500 mm, 3110 mm and 2050 mm, the same as the used SHPB. The contacts between the bars and sample and between the striker and incident bar were defined by AUTOMATIC_SURFACE_TO_SURFACE and AUTOMATIC_SINGLE_ SURFACE, respecttively. The impact velocities in the SHPB direct impact simulations were 10, 20, 30, 60 and 108 m s^{-1}. The models at 10 and 20 m s^{-1} were implemented with 500 mm-long Inconel 718 striker bar, while the tests at 30, 60 and 108 m s^{-1} were implemented using 200 mm-long aluminum striker bar, the same as the tests. The incident and striker bars in these tests were again modeled using 15x2 mm solid elements, whereas aluminum striker bar was modelled using 5x2 mm 10080 solid elements (Figure 1(c)). The contact between the sample and incident bar was defined by AUTOMATIC_SURFACE_TO_SURFACE and the contact between the striker and incident bar was defined by AUTOMATIC_SINGLE_SURFACE. The velocity of striker bar was defined by the VELOCITY_GENERATION card in LS-DYNA. Inconel 718 striker, incident and transmitter bar and aluminum striker bar were simulated using MAT001_ELASTIC material model (Inconel 718: E=207 GPa, v=0.33 and ρ=7850 kg m^{-3} and aluminum: E=71.7 GPa, v=0.33 and ρ=2810 kg m^{-3}). The static and dynamic friction coefficients were taken 0.2 and 0.1 for lubricated surfaces and 0.3 and 0.2 for non-lubricated surfaces, respectively.

The cylindrical AAC sample was modelled using 38400 solid elements and MAT096_BRITTLE_DAMAGE material model. The used material model was also previously applied to simulate the failure of concrete [23]. The material model allowed to admit progressive degradation of tensile and shear strengths across smeared cracks initiated under tensile loads [24]. The compressive failure was governed by a simplistic J2 flow correction [25]. The damage occurred was handled by treating 4-rank elastic stiffness tensor as an evolving internal variable. The main material model parameters are the Elastic modulus, Poisson's ratio, the initial principal tensile strength (f_n), the initial shear traction (f_s), the fracture toughness of the material (g_c), shear retention factor (β), the viscosity of the material (η) and uniaxial compressive yield stress (σ_y) [26]. ERODING_SINGLE_SURFACE was applied to AAC sample by MAT000_ADD_EROSION parameter in both SHPB and direct impact test models. The volumetric-failure-strain (corresponding to compressive strength) at a quasi-static strain rate (0.0117) was used as the erosion parameter in MAT_ADD_EROSION. The volumetric strain (Δ) is

$$\Delta = \varepsilon_x + \varepsilon_y + \varepsilon_z \qquad (2)$$

where ε_x, ε_y and ε_z are the normal strains in x, y and z-axis. The model stresses were determined at the distal-end and impact-end contact areas, at the center and surface elements at the contact areas and on the incident bar at the strain gage location of the test (Figure 1(d)). The determined material parameters of AAC are tabulated in Table 1.

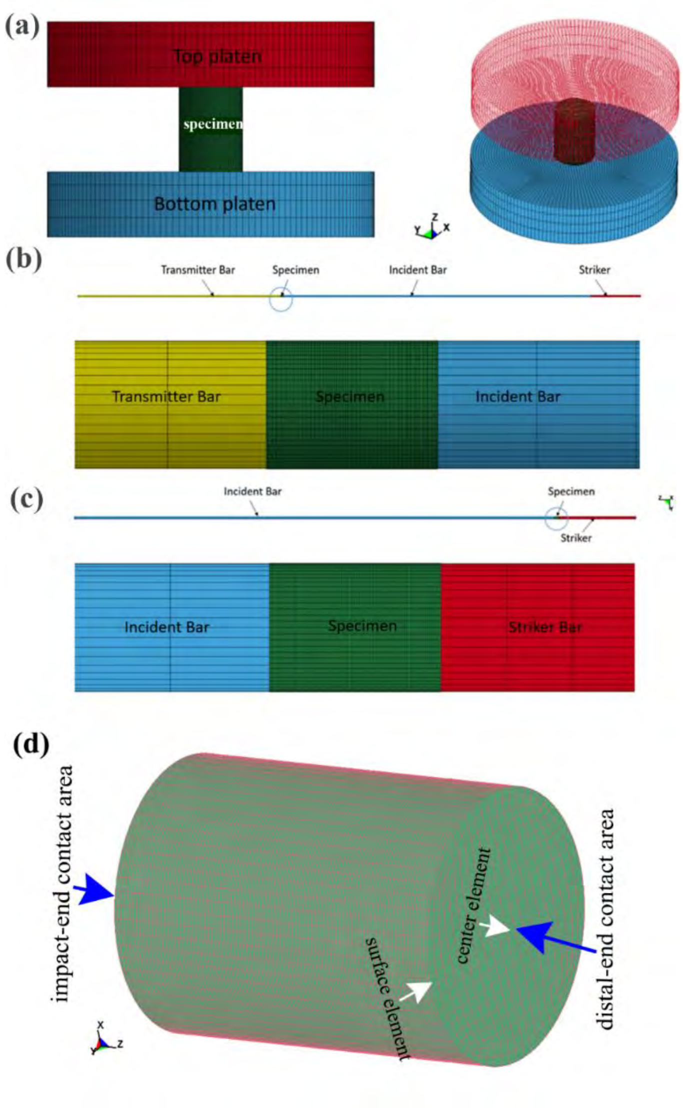

Fig. 1. 2D and 3D models of (a) quasi-static compression, (b) SHPB compression, (c) SHPB direct impact tests and (d) sample with the location of numerical stress measurement

Table 1. Material model parameters of AAC

Parameter	Value
Density, ρ (kg m^{-3})	600
Young's Modulus, E_B (GPa)	0.32
Poisson's Ratio, $\boldsymbol{v}$	0.2
Tensile Limit (MPa)	1
Shear Limit (MPa)	2.56
Compressive yield stress (MPa)	5.11
Fracture Toughness (N m^{-1})	3.47
Shear retention factor	0.03

A shear retention factor of 0.03, typical for concrete, was taken from reference [23] and all other material parameters were extracted for the tests at a quasi-static strain rate of 0.002 s^{-1}. The viscosity was taken zero in order to exclude the effect of strain rate in Model 1, while the compression yield stress corresponding to each velocity were entered in the material model for the strain rate sensitive model, Model 2.

Results and Discussion.

Quasi-static and high strain rate tests

Three representative stress-strain curves of quasi-static compression tests at 5x10^{-5} and 5x10^{-3} m s^{-1}, drop-weight compression tests at 1 m s^{-1} and SHPB direct impact tests at 8 m s^{-1} are shown in Figure 2(a). Note that in the SHPB direct impact tests, the stress was measured from a strain gage 1 m away the sample/incident bar contact area. The equilibrium in SHPB test was further checked by using the following relation [27]: $3t_{tr} = \varepsilon_f l/v$; where t_{tr} and ε_f are the transit time ($l/\sqrt{E/\rho}$) and facture strain of the sample and v, l, E and ρ are the impact velocity and the length, elastic modulus and density of sample, respectively. Using ε_f=0.012, l=26 mm, ρ=600 kg m^{-3} and E=0.7 GPa (Figure 2(a)), one can arrive a critical velocity of ~5 m s^{-1} (t_{tr}=22 μs) above which there will be no stress equilibrium in the SHPB test. In the SHPB compression tests at 8 m s^{-1}, an aluminum disc of 1 mm thick and 10 mm in diameter was used as a pulse shaper [9] in the front of the incident bar to attain stress equilibrium. In these tests, the failure time (100 μs) was more than 4 times the wave transit time, showing nearly a stress equilibrium condition and corresponding to a strain rate of 185 s^{-1} at failure strain (Figure 2(b)). While, the tests at 10 m s^{-1} as seen in Figure 2(b) ($\varepsilon_f l/v$=45 μs) and above are non-equilibrium tests. In these tests, the deformation is represented by $\frac{v}{l}t$ instead of strain. Figure 2(c) shows representative equilibrium stress-$\frac{v}{l}t$ curves at 5x10^{-5} and 1 m s^{-1} and representative non-equilibrium stress-strain curves at 10, 30 and 108 m s^{-1}. Non-equilibrium stress-$\frac{v}{l}t$ curves in the same figure are shown for the comparison between compressive stresses. The maximum stresses in the stress-strain curves of Figures 2(a) and in the stress-$\frac{v}{l}t$ curves of Figure 2(c) are taken as the compressive strengths. As noted in the same figures, the compressive strength increases as the velocity increases between 5x10^{-5} to 30 m s^{-1}, while, the compressive strengths at 30 and 108 m s^{-1} are very much similar. The elastic modulus was determined from the initial slopes of the curves, from 5x10^{-5} to 8 m s^{-1}. The elastic modulus increases from ~0.32 GPa at quasi-static velocity to ~0.7 GPa at 8 m s^{-1} (Figure 2(a)). The slopes of stress-$\frac{v}{l}t$ curves of the tests at 30 and 108 m s^{-1} are comparatively lower as these are non-equilibrium tests. The variation of compressive failure strain (corresponding to the compressive strength) with velocity until about 8 m s^{-1} (SHPB compression equilibrium test) is shown in Figure 2(d). The compressive failure strain starts to decrease at 8 m s^{-1} and an average compressive failure strain of 0.017 is taken for the quasi-static tests. Assuming the SHPB test at 8 m s^{-1} is confined state (no lateral expansion of sample), the volumetric fracture strain are calculated for the tests below this velocity. As shown in Figure 2(d), the average volumetric facture strain is about 0.0117 and this value was used in the modelling. Three tensile stress-displacement curves of the Brazilian tests are shown in Figure 2(e), together with the picture of an undeformed and a deformed, centrally-fractured test sample. The mean tensile strength was determined ~1 MPa at 2x10^{-3} s^{-1}. Dynamic tensile fracture tests were also performed in the SHPB at 10 m s^{-1} (not shown here) and the mean tensile strength in these tests increased to ~1.5 MPa, showing a strain rate dependent splitting behavior of tested AAC samples.

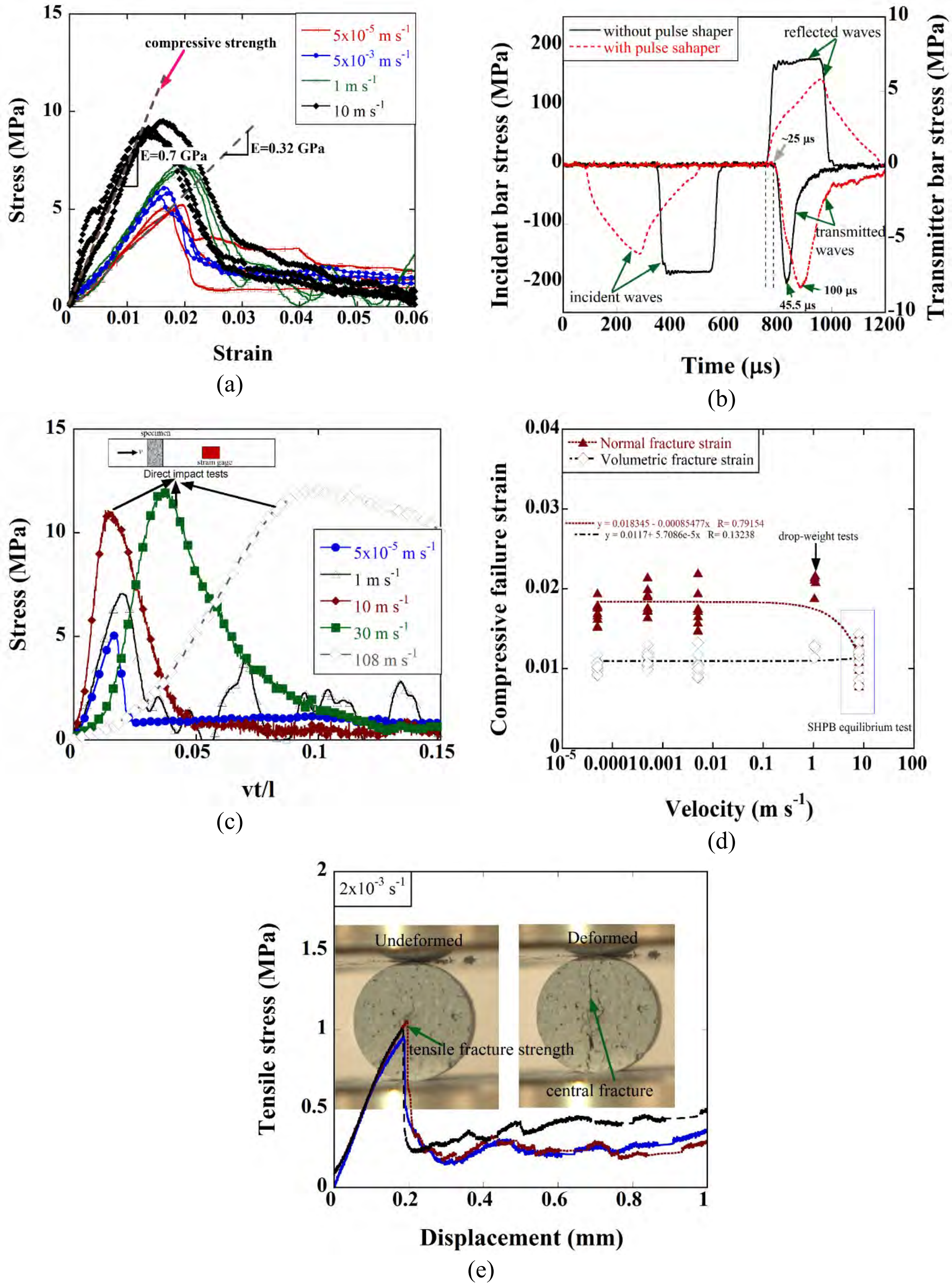

Fig. 2. (a) three stress-strain curves at $5x10^{-5}$, 1 and 10 m s^{-1}, (b) SHPB tests bar stresses with and without pulse shaper at 8 m s^{-1}, (c) typical stress-strain curves at $5x10^{-5}$, 1, 8, 30 and 108 m s^{-1}, (d) the variation of compressive strain with velocity and (e) the quasi-static tensile stress-displacement curves of three Brazilian tests

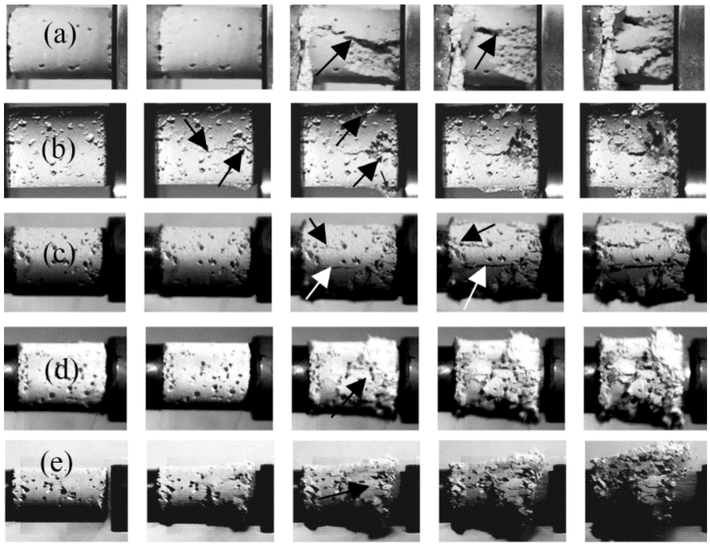

Fig. 3. The deformation pictures of the samples tested at (a)5x10^{-5}, (b)1, (c)10, (d)30 and (e)108 m s^{-1}

The failure at quasi-static velocities occurs by the initiation of a single large axial cracks at the bottom compression test platen as shown by the arrows in Figure 3(a). Additional axial cracks are then formed as the upper compression platen continues to compress the sample until about large displacements.
The samples tested at 1 and 10 m s^{-1} also fail similarly, forming few axial cracks starting at the impact-end and/or striker bar/sample contact area, respectively (Figure 3(b) and (c)). However, the extensive cracking of the sample at the impact-end composing of both axial and radial cracks is seen at 30 and 108 m s^{-1} (Figures 3(d) and (e)). The number of cracks also significantly increase at these velocities, clearly indicating the effect of inertia on the fracture behavior of the tested AAC.

The variation of the compressive strength with strain rate is shown in Figure 4(a) and may be considered in three sequential distinct regions: a lower velocity-dependent strength region (Region 1) at quasi-static and low velocities, a higher velocity-dependent strength region (Region 2) at intermediate velocities between broadly 10 and 30 m s^{-1} and a constant strength region (Region 3), likely above 30 m s^{-1}. These regions are shown by the numbered-circles in Figure 4(a). The International Federation for Structural Concrete (CEB) recommended two empirical equations to define the DIF of concrete strength as [28]

$$DIF = \frac{\sigma_d}{\sigma_s} = \left(\frac{\dot{\varepsilon_d}}{\dot{\varepsilon}_s}\right)^{1.026\alpha} \qquad \dot{\varepsilon_d} \leq 30\ s^{-1} \tag{3}$$

$$DIF = \frac{\sigma_d}{\sigma_s} = \gamma \dot{\varepsilon_d}^{1/3} \qquad \dot{\varepsilon_d} > 30\ s^{-1} \tag{4}$$

where, $\dot{\varepsilon_d}$ and $\dot{\varepsilon}_s$ are the dynamic and static strain rates, respectively. The value of $\dot{\varepsilon_s}$ is 3x10^{-5} s^{-1}, $\gamma = 10^{6.156\alpha-2}$ and $= \frac{1}{(5+\frac{\sigma_s}{10})}$. Fitting the compressive strength values with Eqn. 3, between the lowest quasi-static strain rate and 35 s^{-1} (1 m s^{-1}), and with Eqn. 4 between 35 s^{-1} (1 m s^{-1}) and 1150 s^{-1} (30 m s^{-1}) yield a fracture strength of 4.225 MPa at the reference strain rate, 0.381 for the value of γ and 0.037 for the value of α as depicted in Figure 4(a). As shown in the same figure, the critical strain rate is predicted broadly 100 s^{-1} (~5 m s^{-1}) for rapidly increased compressive strength and 380 s^{-1} (~18 m s^{-1}) or the constant stress region by using Eqn. 4. The compressive strength in Region 2 is also fitted with the following more general equation: $\frac{\sigma_d}{\sigma_s} = \beta \dot{\varepsilon_d}^{n}$, where n=1.113 and β=0.134, resulting in a critical strain rate of ~20 s^{-1} (~1 m s^{-1}) for increased compressive strength in Region 2 and ~760 s^{-1} (~30 m s^{-1}) for the constant stress Region 3. This power equation is noted to be better fitted in Region 2 with the mean DIF values than Eqn. 4 proposed by the CEB as shown in Figure 4(b). A cut-off DIF value of 2.78 above ~1000 s^{-1} (18-30 m s^{-1}) corresponding to a compressive strength of ~11.5 MPa, is also determined for the tested AAC. Figure 4(c) shows the determined compressive strength values of the tested AAC sample using Eqn. 3 at quasi-static velocities and 1, 10, 20, 30, 60 and 108 m s^{-1}. The strength values corresponded to specific test velocities by excluding strength enhancement in Region 2 were used as compressive strength input to the model (Model 2) to determine the strain rate effect on the compressive strength. The experimental mean compressive strength values are further tabulated in Table 2 together with the corresponding velocity and strain rate.

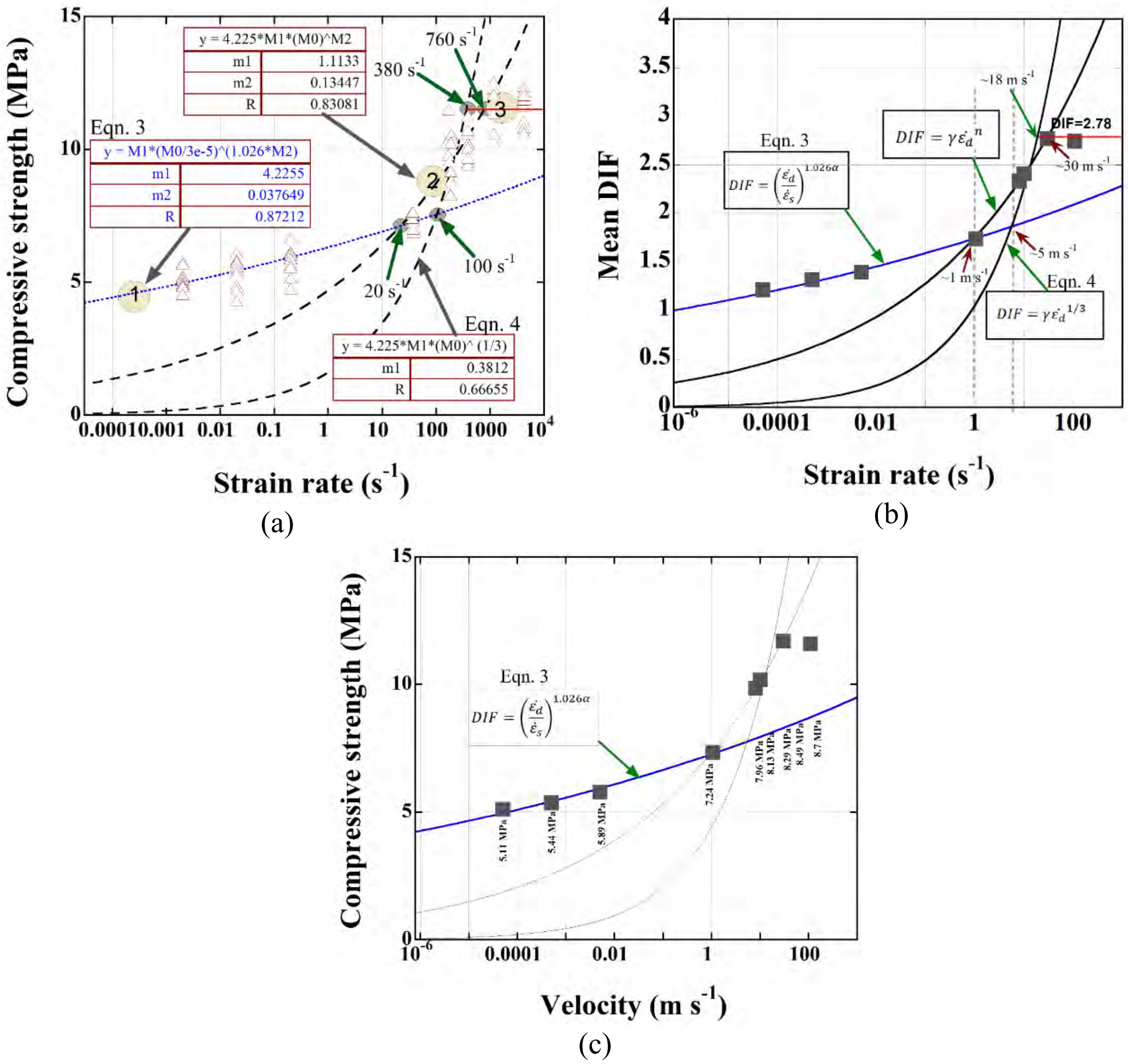

Fig. 4. Experimental (a) compressive strength versus strain rate and fitting with Eqns. 1 and 3, (b) mean DIFs versus velocity and (c) the predicted compressive yield stress of Model 2 at various velocities

Numerical quasi-static and high strain rate compression tests

Figure 5(a) shows the Model 1 numerical stress-$\frac{v}{l}t$ curves at different velocities using a constant compressive strength material model (5. 11 MPa) determined at the quasi-static strain rate of 5x10^{-5} m s^{-1}. Note that only quasi-static compression test at 0.005 m s^{-1} was quasi-statically modelled and the stress in the direct impact SHPB tests were measured both numerically and experimentally 1 m away the sample/incident bar contact area   As similar with experiments, the numerical compressive strength increases with increasing velocity until about 30 m s^{-1}; then it increases slightly with increasing velocity above 30 m s^{-1}. The reduction of the slopes of stress-$\frac{v}{l}t$ curves after about 10 m s^{-1} is also seen numerical stress-$\frac{v}{l}t$ curves but the extent of reduction declines as compared with the tests. The strain gage read numerical compressive strength values are 6, 6.11, 7.2, 8.64, 8.82 and 9.05 MPa sequentially at 1, 10, 20, 30, 60 and 108 m s^{-1}. Compare to experimental strengths tabulated in Table 2, Model 1 numerical compressive strength values are significantly lower at the same velocities.

Table 2. The mean fracture strength of the quasi-static, drop-weight, SHPB and direct impact compression tests

Velocity ($m\ s^{-1}$)	Approximate strain rate (s^{-1})	Test	σ_m (MPa)
$5x10^{-5}$	$2x10^{-3}$	Quasi-static compression	5.11
$5x10^{-4}$	$2x10^{-2}$	Quasi-static compression	5.37
$5x10^{-3}$	$2x10^{-1}$	Quasi-static compression	5.89
1	35	Drop-weight	7.34
8	185	SHPB	9.9
10	385	Direct impact	10.2
30	1150	Direct impact	11.70
108	4150	Direct impact	11.60

When the compression strength is taken strain rate dependent that is the corresponding to compressive strength values at each velocity are input to the material model (Model 2), the numerical compressive strengths increase as seen in Figure 5(b).

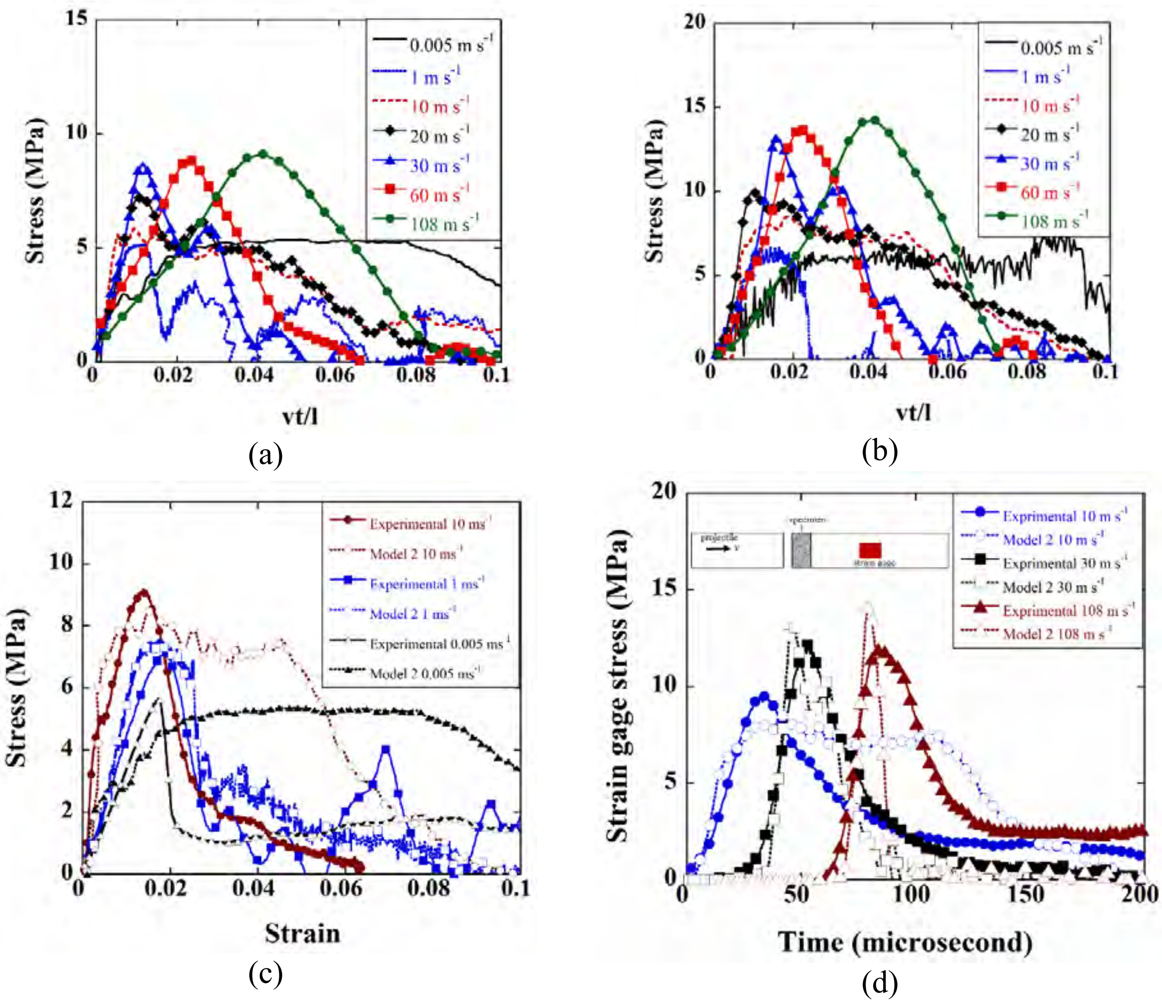

Fig. 5. The numerical stress-strain curves at different velocities; (a) Model 1 and (b) Model 2 and comparison of experimental and model 2 (c) stress-strain and (d) strain gage stress-time curves

Figures 5(c) and 5(d) show the stress-strain and stress-time curves between 0.005 and 8 m s^{-1} and between 10 and 108 m s^{-1}, respectively. The strain gage read numerical compressive strength values in Model 2 increase to 6.4, 6.7, 8.48, 10, 13.1, 13.68 and 14.2 MPa sequentially at 0.005, 1, 10, 20, 30, 60 and 108 m s^{-1} and become much more comparable with the experimental compressive strength values tabulated in Table 2. Also noted in Figures 5(c) and (d), the experimentally measured gage compressive strength values are higher than those of Model 2 until about 10 m s^{-1}; thereafter, Model 2 strength values becomes higher at 30 and 108 m s^{-1}. The post-failure regions of experimental and model curves are also different, Model 2 show a more progressive failure than the experiments. Despite these differences between the gage-measured stress of models and experiments, Model 2 and Model 1 show pretty well the trends of compressive strength variation with velocity. After this verification, the model compressive strength values were determined at the distal-end and impact-end contact areas as well as the elements at the center and surface of the sample at both distal-end and impact-end.

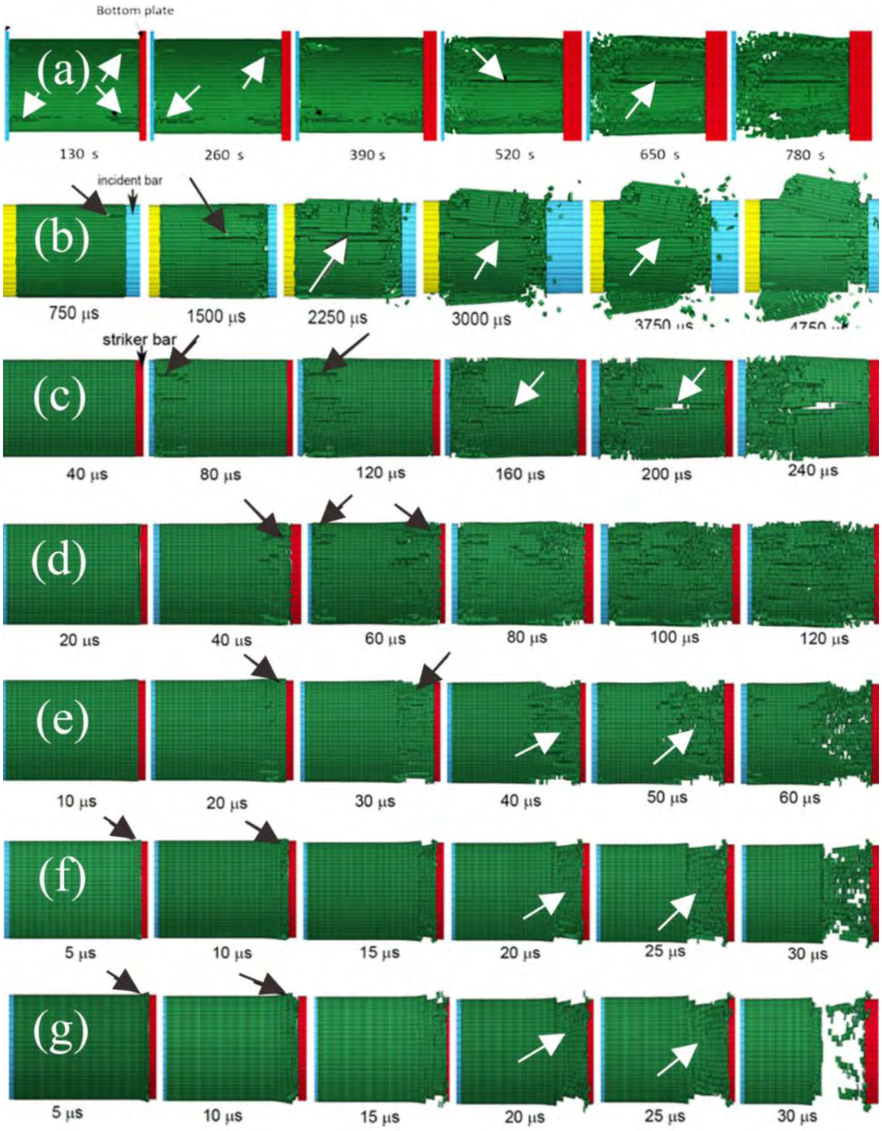

Fig. 6. The numerical deformation pictures of the samples tested at (a)quasi-static, (b)1, (c)10, (d)20, (e) 30, (f) 60, and (g) 108 m s^{-1}

Figures 6(a-g) show Model 1 numerical deformation pictures (at various deformation times) at 0.005, 1, 10, 20, 30, 60 and 108 m s^{-1}, respectively.

The corresponding 3D views of the characteristic damage progression modes (after about compressive strength) between 1 and 108 m s^{-1} are also depicted in Figure 7. As marked by arrows in Figure 6(a-c), the cracks initiate either at one end or at both ends of the samples, while later these initial cracks turn to one or two large axial cracks at increasing times at 0.005, 1 and 10 m s^{-1}. This explained numerical axial cracking behavior also seen in Figure 7 at 1 and 10 m s^{-1}, and is pretty much comparable with the experimental fracture behavior at the same velocities, as depicted in Figure 3. However, the cracks initiate at the impact-end and are proceeded by radial cracking at 20 m s^{-1} and above as shown in Figures 6(d-g) and Figure 7. Again, the numerical facture shows well matching with the experimental facture at 30 and 108 m s^{-1} shown in Figure 3. Model 2 deformation and failure modes at varying velocities were also found very similar with Model 1, except the facture occurred at higher stresses.

Figure 8 shows the variation of numerical distal-end DIFs with the logarithm of velocity. In the same figure, the experimentally measured strain-gage DIFs are also shown for comparison. A rapid increase in the experimental and numerical DIFs after about 1 m s^{-1} is clearly seen in the same figure. The increase in the DIFs is noted to continue until about 30 m s^{-1}. The experimental DIFs however show a sudden cut-off at about 30 m s^{-1}, while both Model 1 and Model 2 DIFs increase with increasing velocity above 30 m s^{-1}. The DIFs of Model 1 however increases relatively slowly above 30 m s^{-1}, while the increase in Model 2 is comparably higher. This difference is attributed to the velocity dependent compressive yield stress used in Model 2. As Model 1 uses a constant compressive yield stress it shows merely the effect of axial and radial inertia on the DIF values, while Model 2 shows both the effects of inertia and strain rate. The modeling results tend to conclude that inertia is effective with increasing velocity between 1 and 30 m s^{-1}. Experimentally, it is presumed that AAC sample reaches a shock compressive strength in Region 2 without entering Region 3. A similar conclusion may be made for Model 1. While, in Model 2, the compressive yield stress also increases in Region 3. Although Model 1 resembles the experimental DIFs by a constant compressive strength in Region 3, Model 2 resembles the experimental DIFs in both Region 1 and Region 2. Nevertheless, both models show an "s-type" DIF-velocity graph, proving the transformation of the deformation state form 1D stress to 1D strain. Lastly, although the proposed power law equation shows well matching with the experimental and model DIFs at lower velocities in Region 2, Eqn. 4 better predicts Model 2 DIFs at higher velocities, ~30 m s^{-1}.

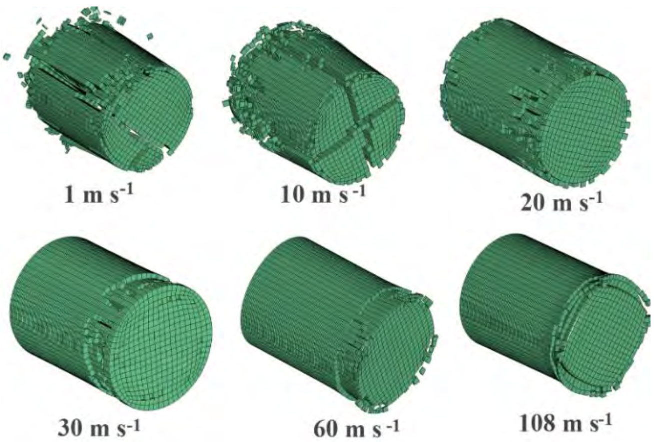

Fig. 7. Model 1 numerical failure modes at different velocities

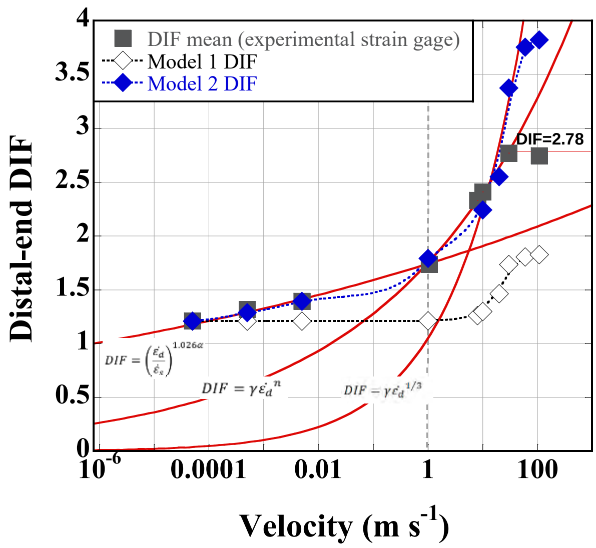

Fig. 8. The variations of experimental and numerical DIFs and numerical contact stresses with velocity

Figures 9 (a-e) show the variation of Model 1 impact-end, distal-end and distal–end center and surface element stresses with time sequentially at 1,10, 20, 30 and 60 m s^{-1}. The element stresses were determined from the selected center and surface element at the distal-end, while impact-end and distal-end stresses were calculated from all elements at the surface of the sample. The time difference between the impact and distal-end stresses in the same figures is due to the wave-transit-time of AAC sample. Figures 9(a-e) clearly indicate that the impact-end and distal-end stresses are similar until about 20 m s^{-1}, while the center and surface element stresses starts to differentiate at about 10 m s^{-1}. The center element stress is higher than the surface element stress until about 20 m s^{-1}, then the surface element stress increases over that of the center element stress at higher velocities, proving the transformation of the failure from an axial to a radial fracture.

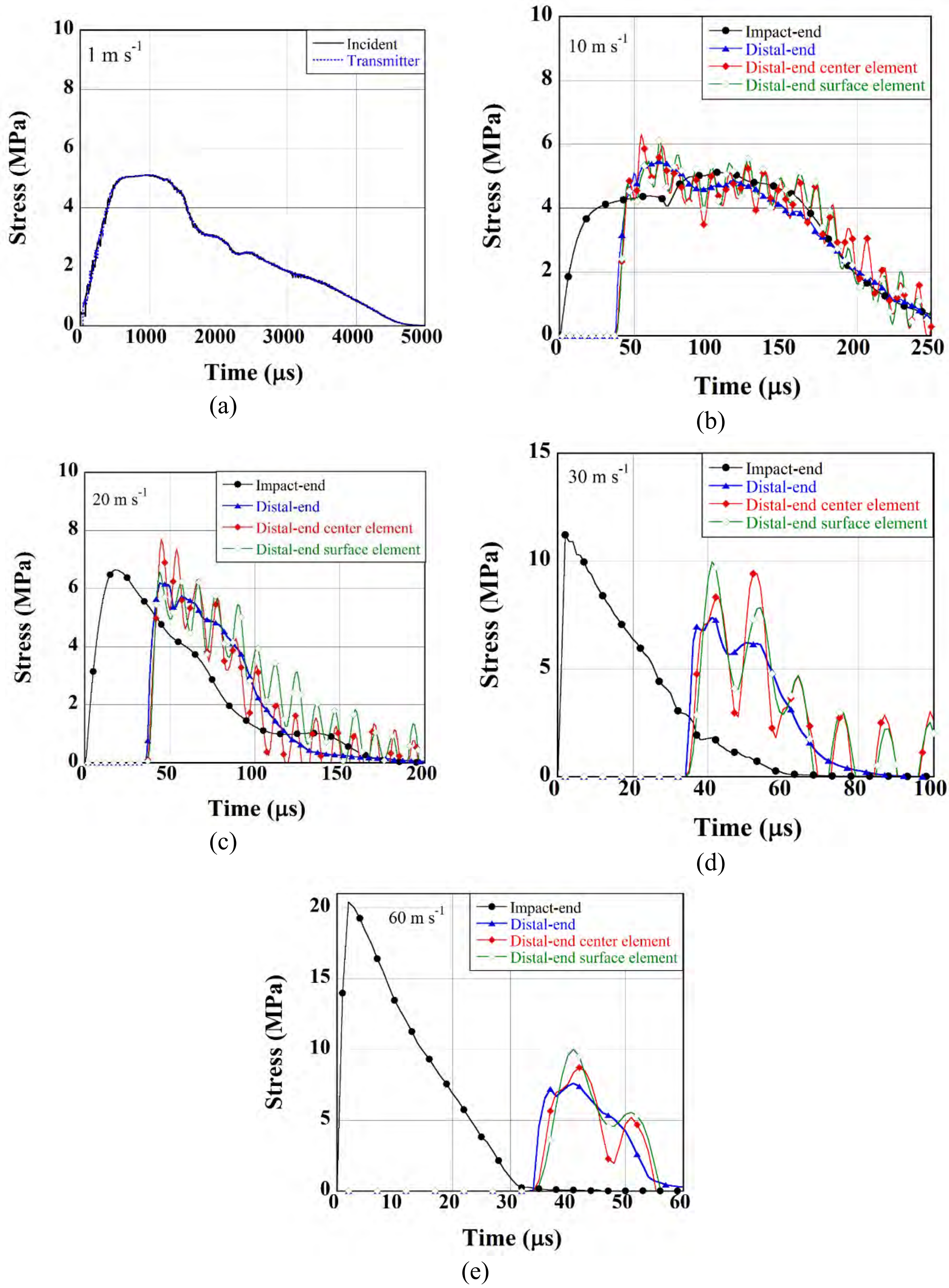

Fig. 9. The variation of Model 1 impact-end, distal-end, distal–end center and surface element and strain gage location stresses with time at (a)1, (b)10, (c) 20, (d) 30 and (e) 60 m s^{-1}

The stress triaxiality is defined as

$$\eta_{1D\ stress} = \frac{\sigma_x+\sigma_y+\sigma_z}{3\sigma_{eq}} \quad (5)$$

where σ_x, σ_y and σ_z are stresses on x, y and z directions and σ_{eq} is equivalent stress. The equivalent stress is

$$\sigma_{eq} = \frac{1}{\sqrt{2}}\left[\left(\sigma_x - \sigma_y\right)^2 + \left(\sigma_y - \sigma_z\right)^2 + (\sigma_z - \sigma_x)^2 + 6(\tau_{xy}^2 + \tau_{yz}^2 + \tau_{xz}^2)\right]^{\frac{1}{2}} \tag{6}$$

Since $\sigma_{eq} = \sigma_x$ in the quasi-static test, $\eta_{1D\ stress} \approx 0.33$. Assuming fully confined elastic state at high strain rates, the stress triaxiality is

$$\eta = \frac{1+\nu}{3(1-2\nu)} \tag{7}$$

By taking the Poisson's ratio equals to 0.2, the stress triaxiality approaches to ~0.66 for a full 1D state of strain. Figure 10 shows the Model 1 and Model 2 distal-end and impact end DIFs together with the Model 1 impact-end surface element stress triaxiality (non-eroded element). The numerical stress triaxiality increases with increasing velocity after about 10 m s^{-1} (35 s^{-1}) and reaches a steady value of 0.66 at about 30 m s^{-1} (marked by an arrow in Figure 10). The result clearly indicates a full uniaxial state of strain attainment in the numerically tested samples after about 30 m s^{-1} (1000 s^{-1}). Modelling SHPB tests on a concrete using a pressure dependent strength model previously showed a stress triaxiality (η) was near 1D state of stress ($\eta = -0.33$) at 47 s^{-1}, while it reached 1D state of strain ($\eta = -0.66$) at ~795 s^{-1} when $\nu = 0.2$ [15]. Above this critical strain rate, the sample deformation was completely 1D state of strain. Furthermore, the critical strain rate for the passage to 1D state of strain was shown to depend on the diameter of sample, larger diameter samples showed larger inertial effects hence lower critical strain rate for the complete 1D state of strain [15]. In the present study relatively small samples were used, 19.4 mm in diameter and 26 mm in length. The transformation strain rate from the uniaxial state of stress to the uniaxial state of strain is found 1150 s^{-1}, which is also very much consistent with the previous numerical simulations on concrete [15].

Assuming cellular concrete deforms in 1D state of strain by forming a shock front depicted in Fig. 11, the impact end-stress (σ^*) is governed by the following rigid-perfectly-plastic-locking (r-p-p-l) model, based on mass and momentum conservation as [29],

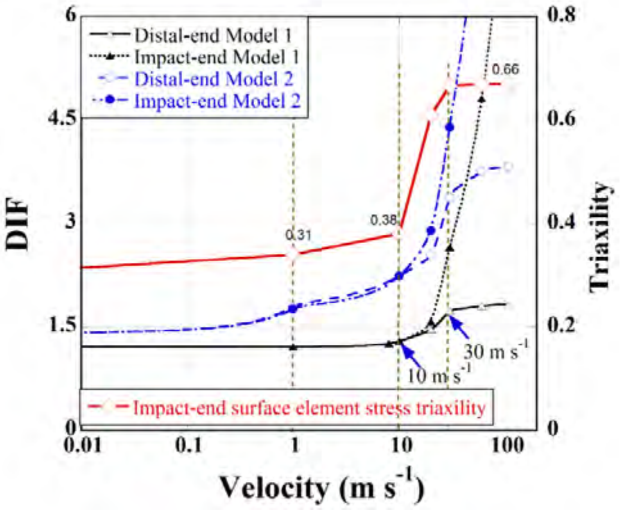

Fig. 10. Experimental and numerical DIFs together with distal-end stress triaxiality

$$\sigma^* = \sigma_p + \frac{\rho_o}{\varepsilon_d} v_o^2 \tag{8}$$

In above equation, σ_p is the plateau stress, v_o is the initial velocity, ρ_o is the initial density and ε_d is the densification strain. The plateau stress of present AAC sample is determined using Eqn. 3 for the strain rate sensitive case (Model 2) as

$$\sigma_p = \sigma_s \left(\frac{v}{v_s}\right)^{1.026\alpha} \tag{9}$$

where, v is the impact velocity and v_s is the reference velocity corresponding to the reference strain rate. The determined experimental values of σ_s and v_s are 4.225 MPa and 7.8x10^{-7} m s^{-1}, respectively. A constant plateau stress of 5.11 MPa is taken for the strain rate insensitive case (Model 1). The densification strain was determined from confining compression tests on AAC samples. Simply, a cylindrical sample was tightly fitted inside a cylindrical tube, then the sample was compressed with a flat end punch. Figure 11(a) shows the confinement stress-strain curves of these tests together with the picture of tested sample before and after the test. The densification of the sample is clearly seen in these pictures, showing a nearly full confined state. The densification strain is determined 0.28 by using a liner intercept method as shown in Figure 11(a).

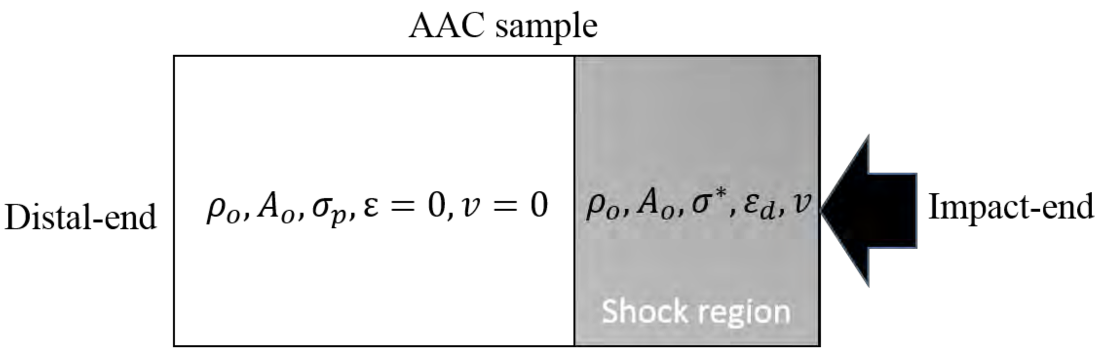

Fig. 11. Schematic of shock formation in AAC sample

The predicted impact-end stresses using Eqn. 8 and Eqn. 9 are shown as function of the logarithm of velocity in Figure 11(b) and (c) together with experimental and numerical distal-end and impact end DIFs, respectively. The predictions result in critical velocities near 10 m s^{-1} for the increased impact-end stresses for 1D state of strain as shown in the same figures. This also shows a good match with the experimental and numerical results.

Conclusions. The effect of inertia and strain rate on the failure of a cellular concrete (600 kg m^{-3}) was investigated using a constant volumetric-failure-strain erosion criterion in LSDYNA. Two modelling approach, namely rate insensitive (constant compressive yield stress) and rate sensitive (variable compressive yield stress) were implemented and the results were compared with the experimental compression tests performed at similar strain rates, between 2x10^{-3} s^{-1} and ~4150 s^{-1}. The effect of inertia in increasing the compressive strength of cellular concrete at increasing strain rates was shown both experimentally and numerically. An “s-type” compressive strength relation with strain rate was also found, composing of three different distinct regions: a lower velocity-dependent strength region at the quasi-static velocities (Region 1), a higher velocity-dependent strength region at intermediate velocities (Region 2) and again a lower velocity-dependent strength region above about 1150 s^{-1} (Region 3). In experimentally tested samples, a shock compressive strength was presumed to be reached in Region 2 or just at the beginning of Region 3, resulting in a cut-off DIF value (2.78), while in numerically tested samples, the compressive strength (Model 2) increased even in Region 3 with a rate very much similar to that of Region 1. One dimensional state of strain condition above a critical velocity was also shown numerically and the stress triaxiality increased to 0.66 within 1 and 30 m s^{-1}, reaching a fully constraint 1D state of strain condition above 30 m s^{-1}. In accord with this, the numerical fracture mode, as with the experiments, switched from an axial-dominated to a radial-dominated cracking after about 20 m s^{-1}. A simple shock analysis also proved 1D state of strain after about 10 m s^{-1}. Finally, the strain rate dependent compressive strength was numerically presented as partly due to the change of the deformation state from a 1D state of stress to an1D state of strain and partly due to the intrinsic rate sensitivity of cellular concrete.

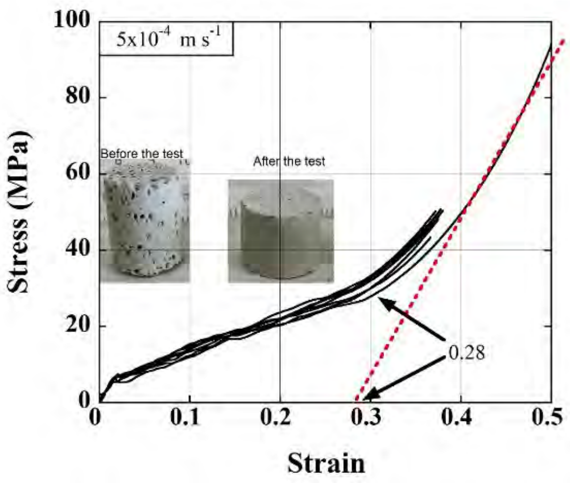

(a)

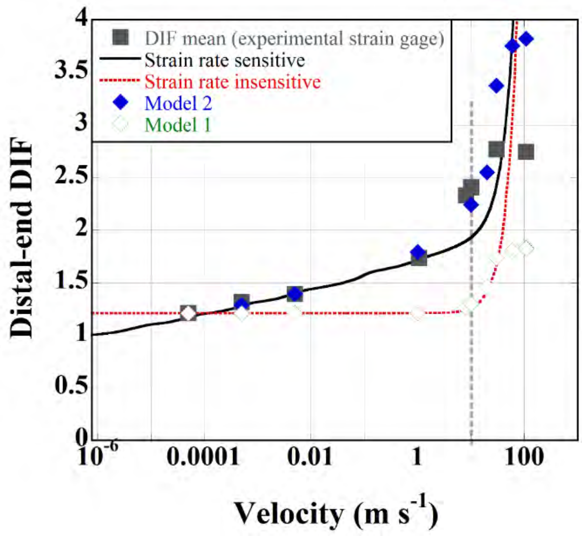

(b)

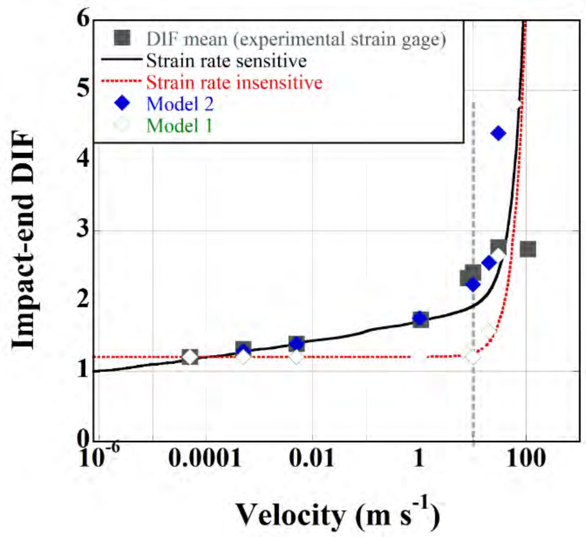

(c)

Fig. 12. (a) confined compression stress-strain curves and (b) distal-end and (c) impact-end stress prediction based on r-p-p-l model

Acknowledgement.

Authors would like to thank AKG Gaz Beton of Turkey for providing AAC blocks for the present study.

REFERENCES

[1]. Khosravani, M.R., Weinberg, K. *A review on split Hopkinson bar experiments on the dynamic characterisation of concrete.* Construction and Building Materials, 2018, 190, pp. 1264-1283.
[2]. Bischoff, P.H., Perry, S.H. *Compressive behavior of concrete at high-strain rates.* Materials and Structures, 1991, 24, 425-450.
[3]. Zhang, Q.B., Zhao, J. *A Review of Dynamic Experimental Techniques and Mechanical Behaviour of Rock Materials.* Rock Mechanics and Rock Engineering, 2014, 47, pp. 1411-1478.
[4]. Lu, D.C., Wang, G.S., Du, X.L., Wang, Y., 2017. *A nonlinear dynamic uniaxial strength criterion that considers the ultimate dynamic strength of concrete.* Int. J. Impact Eng., 2017, 103, pp. 124-137.

[5]. Rossi, P., Toutlemonde, F.J.M. *Effect of loading rate on the tensile behaviour of concrete: description of the physical mechanisms.* Materials and Structures, 1996, 29, pp. 116-118.

[6]. Brace, W.F., Jones, A.H. *Comparison of uniaxial deformation in shock and static loading of three rocks.* Journal of Geophysical Research, 1971, 76, pp. 4913-4921.

[7]. Zeng, S.J., Ren, X.D., Li, J. *Triaxial Behavior of Concrete Subjected to Dynamic Compression.* Journal of Structural Engineering, 2013, 139, pp. 1582-1592.

[8]. Legeron, F., Paultre, P. *Uniaxial confinement model for normal- and high-strength concrete columns.* Journal of Structural Engineering-Asce, 2003, 129, pp. 241-252.

[9]. Sfer, D., Carol, I., Gettu, R., Etse, G. *Study of the behavior of concrete under triaxial compression.* Journal of Engineering Mechanics-Asce, 2002, 128, pp. 156-163.

[10]. Lahlou, K., Lachemi, M., Aitcin, P.C. *Confined high-strength concrete under dynamic compressive loading.* Journal of Structural Engineering-Asce, 1999, 125, pp. 1100-1108.

[11]. Li, X.G., Liu, Z.L., Lv, Y., Cai, L.X., Jiang, D.B., Jiang, W.G., Jian, S.W. *Utilization of municipal solid waste incineration bottom ash in autoclaved aerated concrete.* Construction and Building Materials, 2018, 178, pp. 175-182.

[12]. Lee, S., Kim, K.M., Park, J., Cho, J.Y. *Pure rate effect on the concrete compressive strength in the split Hopkinson pressure bar test.* Int. J. Impact Eng., 2018, 113, pp. 191-202.

[13]. Grady, D.E., 1998. *Shock-wave compression of brittle solids.* Mechanics of Materials, 1998, 29, pp. 181-203.

[14]. Yu, S.S., Lu, Y.B., Cai, Y. *The strain-rate effect of engineering materials and its unified model*. Latin American Journal of Solids and Structures, 2013, 10, pp. 833-844.

[15]. Liu, F., Li, Q.M. *Strain-rate effect on the compressive strength of brittle materials and its implementation into material strength model*. Int. J. Impact Eng., 2019, 130, pp. 113-123.

[16]. Yankelevsky, D.Z., Avnon, I., 1998. *Autoclaved aerated concrete behavior under explosive action*, Construction and Building Materials, 1998, 12, pp. 359-364.

[17]. Serrano-Perez, J.C., Vaidya, U.K., Uddin, N. *Low velocity impact response of autoclaved aerated concrete/CFRP sandwich plates.* Composite Structures, 2007, 80, pp. 621-630.

[18]. Mespoulet, J., Plassard, F., Hereil, P.L., *Strain rate sensitivity of autoclaved aerated concrete from quasi-static regime to shock loading.* Dymat 2015 - 11th International Conference on the Mechanical and Physical Behaviour of Materials under Dynamic Loading, E D P Sciences, Cedex A.

[19]. Nian, W., Subramaniam, K.V., Andreopoulos, Y. *Experimental investigation on blast response of cellular concrete*. Int. J. Impact Eng., 2016, 96, pp. 105-115.

[20]. Odac, I.K., Guden, M., Klcaslan, C., Tasdemirci, A. *The varying densification strain in a multi-layer aluminum corrugate structure: Direct impact testing and layer-wise numerical modelling.* Int. J. Impact Eng., 2017, 103, pp. 64-75.

[21]. Sankaya, M., Tasdemirci, A., Guden, M. *Dynamic crushing behavior of a multilayer thin-walled aluminum corrugated core: The effect of velocity and imperfection*. Thin-Walled Struct., 2018, 132, pp. 332-349.

[22]. Sarikaya, M., Tasdemirci, A., Guden, M. *Impact loading and modelling a multilayer aluminium corrugated/fin core: The effect of the insertion of imperfect fin layers*. Strain, 2019, 55, p. 17.

[23]. Li, Z., Chen, L., Fang, Q., Hao, H., Zhang, Y., Chen, W., Xiang, H., Bao, Q. *Study of autoclaved aerated concrete masonry walls under vented gas explosions*. Engineering Structures, 2017, 141, pp. 444-460.

[24]. Oliver, J., 1989. *A consistent characteristic length for smeared cracking models.* International Journal for Numerical Methods in Engineering, 1989, 28, pp. 461-474.

[25]. Govindjee, S., Kay, G.J., Simo, J.C. *Anisotropic modeling and numerical-simulation of brittle damage in concrete.* International Journal for Numerical Methods in Engineering, 1995, 38, pp. 3611-3633.

[26]. Halquist, J. *LS-DYNA keyword user's manual version 971.* Livermore Software Technology Corporation, 2007, Livermore, CA.
[27]. Ravichandran, G., Subhash, G. *Critical-appraisal of limiting strain rates for compression testing of ceramics in a split hopkinson pressure bar.* Journal of the American Ceramic Society, 1994, 77, pp. 263-267.
[28]. CEB, *Concrete structures under impact and impulsive loading.* Bulletin d'information, 1998, No 187, CEB Comite´ EuroInternational du Be´ton, Lausanne.
[29]. Reid, S.R., Peng, C. *Dynamic uniaxial crushing of wood*. Int. J. Impact Eng., 1997, 19, pp. 531-570.

Received: 14.08.2022
Accepted: 03.11.2022